JGR Space Physics

DATA ARTICLE
10.1029/2025JA034252

Key Points:

- The largest MMS shock data set with burst-mode data is made publicly available and analyzed using both multi-spacecraft timing and modeling
- Discrepancies emerge between local and global shock properties, favoring quasi-perpendicular geometries even amid upstream foreshock
- Modeled shock properties better match theoretical expectations, highlighting the limitations of deriving local shock characteristics

Correspondence to:
V. Toy-Edens,
vicki.toy-edens@jhuapl.edu

Citation:
Toy-Edens, V., Raptis, S., Turner, D. L., Mo, W., & Young, S. A. Q. (2025). Automated bow shock identification and multi-spacecraft timing using magnetospheric multiscale (MMS) observations. *Journal of Geophysical Research: Space Physics*, *130*, e2025JA034252. https://doi.org/10.1029/2025JA034252

Received 30 MAY 2025
Accepted 22 SEP 2025

Automated Bow Shock Identification and Multi-Spacecraft Timing Using Magnetospheric Multiscale (MMS) Observations

Vicki Toy-Edens[1], Savvas Raptis[1], Drew L. Turner[1], Wenli Mo[1], and Sean A. Q. Young[1]

[1]Johns Hopkins University Applied Physics Laboratory, Laurel, MD, USA

Abstract Utilizing 8 years of dayside Magnetospheric Multiscale (MMS) mission plasma region identifications, we present an automatically identified and manually verified data set of 2,594 bow shock crossings in MMS burst-mode. For each bow shock crossing, we identify the bow shock ramp in each MMS probe using two automated methods and apply multi-spacecraft timing to calculate the bow shock normal. The bow shock list was separated into quasi-parallel and quasi-perpendicular based on the presence or absence of ion foreshock in order to evaluate deviations between the automated methods and a statistical 3D bow shock model. There are large discrepancies between global and local shock properties where the local shock properties are highly skewed towards quasi-perpendicular properties regardless of the presence of ion foreshock. Although this skewness grows when the tetrahedral configuration is suboptimal, it persists even under ideal formation, indicating that electron-scale processes can modulate local shock properties. These findings highlight the limitations of local multi-spacecraft timing in accurately characterizing shock geometry without contextual information, such as the presence of an upstream foreshock or a similarly disturbed downstream magnetosheath. Ultimately, this data article provides thousands of high-resolution bow shock crossings for further scientific research by the community.

1. Introduction

Collisionless shocks are one of nature's most efficient particle accelerators and are considered the underlying process driving cosmic rays (Caprioli & Spitkovsky, 2014; Park et al., 2015; Raptis et al., 2025; D. Turner et al., 2018; L. B. Wilson et al., 2016). While they have been studied for almost a century, the physics that dictates the evolution and dynamics of collisionless shocks is not fully understood (Balogh & Treumann, 2013; R. Treumann, 2009). Characterizing the geometry of a planetary bow shock is crucial for understanding the physical effects on particles. The dynamical evolution of a shock with a normal vector nearly parallel (quasi-parallel or Qpar) to the upstream magnetic field differs significantly from that of a shock where the field is nearly perpendicular (quasi-perpendicular or Qperp) (Balogh & Treumann, 2013). In Qpar shocks, one expects the presence of an upstream ion foreshock region filled with Ultra Low Frequency (ULF) waves and various nonlinear localized pulses such as Short Large Amplitude Magnetic Structures (SLAMS) and shocklets. This environment is driven by reflected particles from the supercritical shock, and since the magnetic field is nearly parallel, these particles travel upstream and interact with the incoming solar wind. This interaction produces a highly turbulent environment both upstream and downstream of the shock, extending its influence over large spatial scales (Eastwood et al., 2005). Conversely, Qperp shocks are typically less turbulent since particles briefly gyrate at the shock transition before being convected downstream. This simpler dynamic generally leads to the absence of an ion foreshock and a more limited range of phenomena governed primarily by ion kinetic scales. Despite this separation, shocks are inherently non-stationary and, regardless of their geometry, can exhibit phenomena such as rippling (Johlander et al., 2016) and shock reformation (Liu et al., 2021; Raptis et al., 2022; D. L. Turner et al., 2021), which can alter the shock properties locally.

To characterize the shock geometry, we typically use the angle between the local shock normal and the upstream interplanetary magnetic field (IMF), resulting in an angle (θ_{Bn}) that ranges from 0 to 45° for Qpar shocks, and to 45–90° for Qperp shocks. Although there are several methods to estimate this angle, the approach largely depends on the available in situ observations and the expected scales governing the shock transition. Typically, calculating θ_{Bn} requires estimating the normal vector $\hat{\mathbf{n}}$, which can be achieved using various methods. These include shock timing across the four spacecraft (Russell et al., 1983), techniques that utilize local measurements combined with predictions of plasma and magnetic field variability across the shock (single spacecraft methods; Schwartz, 1998;

Trotta et al., 2022), or approaches based on a global bow shock model (Schwartz, 1998). In addition, one must obtain the upstream magnetic field vector (**B**), which for Earth's bow shock is usually derived either from propagated solar wind values (e.g., OMNIweb data; King & Papitashvili, 2005) or from upstream in situ spacecraft observations during the shock crossing.

Previous efforts on systematic shock characterization (e.g., Lalti et al., 2022) have employed techniques that rely on the magnetohydrodynamic (MHD) description of the shock, propagated solar wind data, and modeling efforts to estimate the local θ_{Bn}. Their analysis, similar to ours, utilized Magnetospheric Multiscale (MMS Burch et al., 2015) mission observations, typically obtained in very close formation (<50 km), making this approach optimal once the exact shock crossing is manually determined. However, their method did not include a robust and automatic determination of the shock ramp and relied on survey/fast MMS data. Similarly, while previous case studies (e.g., Gingell et al., 2017; Johlander et al., 2016) have highlighted the limitations of multi-spacecraft techniques for shocks, no systematic effort has been made to statistically evaluate these limitations across different shock geometries.

Looking locally at in situ observations of shocks, Karlsson et al. (2021), using ESA's Cluster observations, demonstrated that foreshock signatures can be observed at shock crossings with θ_{Bn} above 45° and up to approximately 60°. This result, obtained by analyzing typical in situ properties upstream (foreshock) and downstream (magnetosheath) of Qpar shocks, has proven effective and has been extensively used in the last 5 years (Karlsson et al., 2021; Koller et al., 2024; Raptis, Aminalragia-Giamini, et al., 2020; Raptis, Karlsson, et al., 2020; Svenningsson et al., 2025). A direct implication of this finding is that while strictly speaking Qpar shock crossings should correspond to angles below 45°, the influence of foreshock dynamics can extend into more oblique shock geometries ($40° \leq \theta_{Bn} \leq 60°$). However, this relationship has not been evaluated with data sets other than that of Karlsson et al. (2021) and has not been statistically examined for a range of upstream conditions. Additionally, the structure of Qpar shocks is characterized by steepened ULF waves (e.g., SLAMS and shocklets), which drive the reformation of Qpar shocks (Johlander et al., 2022; Raptis et al., 2022). These ion-scale phenomena are most prominent upstream of Qpar shocks (Bergman et al., 2025), and they can act locally as Qperp shocks. This means that upstream of them, out-of-plane whistler waves can be found which may modify the local shock geometry toward more perpendicular orientations (Baumjohann & Treumann, 2012; Liu et al., 2021; Raptis et al., 2022; R. A. Treumann & Baumjohann, 1997; L. Wilson et al., 2013).

In this data article, we present the first fully automated shock ramp determination using burst-mode data from the MMS mission, along with the calculation of the shock speed and bow shock vector through multi-spacecraft timing. By employing a novel methodology to a pre-existing data set (Toy-Edens, 2024), we provide the largest burst shock data set openly available to the community. Additionally, to demonstrate the applicability of our data set we perform fully automated multi-spacecraft timing using two different methods and compare the results with model-driven shock geometry parameters, thereby simultaneously investigating local and global shock geometries. Our analysis reveals certain caveats in timing processes when evaluating collisionless shocks, and we offer suggestions for future missions.

2. Data

In this work, our goal is to characterize MMS shock crossings that have burst data available. Specifically, we utilize Level 2 MMS data in burst mode from the Fast Plasma Investigation (FPI, Pollock et al., 2016) and Fluxgate Magnetometers (FGM, Torbert et al., 2014) to automate bow shock identification in high MMS temporal resolution data. We use the ion moments data (omni-directional flux, density, and velocity) from the four FPI ion spectrometers at a temporal resolution of 150 ms (opposed to the survey mode resolution of 4.5 s) and the FGM magnetic field vector. Level 2 survey Magnetic Ephemeris and Coordinates (MEC, Henderson et al., 2022) ephemeris data (`epht89d`) provides the location of the spacecraft at a temporal resolution of 30 s. We proceed to interpolate the MEC data to match the high temporal burst data to identify the spatial location of the bow shock. Finally, we note that we consider the effects of aberration of the bow shock location in the data. Therefore, we aberrate the coordinates considering the effects of the X component of the mean solar wind velocity from a 10-min window around the bow shock epoch from OMNI high-resolution 1-min cadence data (King & Papitashvili, 2005). As a result, our coordinate system is the aberrated Geocentric Solar Ecliptic (aGSE).

Additionally, for parts of our analysis, we utilize the MMS tetrahedron quality factor (Q; Fuselier et al., 2014) which is a measurement from 0 to 1 describing how close to a tetrahedron formation the four spacecraft are. Q takes into account both the shape of the configuration through tetrahedron volume ratios and the variation in separation lengths between probes. When Q is 1, it is in the most optimal tetrahedron configuration, while when it is 0 it is in the least optimal configuration. This metric allows us to evaluate if our multi-point timing calculations are sensitive to how well the MMS probes are flying in formation.

Our work uses a list of shock crossings from Toy-Edens et al. (2024). In that work, an automated unsupervised machine learning approach used MMS Level 2 survey/fast data to classify 8 years of dayside ($X_{GSE} > 0$) observations into four plasma regions (magnetosphere, magnetosheath, solar wind, and ion foreshock). The resultant data set (Toy-Edens, 2024) also contained plasma transitions (magnetopause, Qpar bow shock, and Qperp bow shock) based on when the spacecraft changed from one plasma region to another. A Qperp crossing was marked when the spacecraft environment changed from magnetosheath to solar wind or vice versa, while a Qpar crossing was obtained when the environment labeled changed from magnetosheath to ion foreshock or vice versa. Toy-Edens et al. (2024) reports 23,801 bow shocks across all four MMS probes from September 2015 through 31 January 2024 that we use for our study's initial temporal bow shock identifications. To remove incorrectly labeled bow shock crossings, we require that all four probes have identified a bow shock crossing within 3 min of one another and that there are no magnetosphere classifications within ±5 min of the crossing. Combining these filters reduces the bow shock list to a total of 5,157 distinct bow shock crossings across all MMS probes. Finally, when we require that burst mode data are available for all four probes, we have a total of 2,594 dayside bow shock crossings in aGSE coordinates. The timing and spatial location of each shock ramp is made publicly available (see Section 5).

Throughout this study, we compare bow shock normals to statistical 3D bow shock models based on Monte Carlo simulations of solar wind conditions from 27 years of OMNI data using the Chapman and Cairns (2003) bow shock model from Yeakel et al. (2025). We also account for aberration in the bow shock model boundary assuming an average 4° aberration.

3. Methodology

We identify bow shock ramps in the MMS burst mode data with two methods: the first is through a series of sigmoid fittings and thresholds applied to each MMS probe (Section 3.1) and the second uses the bow shock location from the first method in MMS2 and performs cross-correlation to find the location in the remaining MMS probes (Section 3.2). We calculate the bow shock normal using multi-point timing (Section 3.3) based on the crossing times obtained from both methods.

3.1. Method 1: Sigmoid MMS Bow Shock Identification

Method 1 utilizes sigmoid fitting alongside thresholds of ratios between pre- and post-transition mean values. The primary sigmoid fit is conducted on ion number density (n_{ion}) to determine the time of each bow shock crossing. Additional filters are added to remove unphysical variations of n_{ion} that do not correspond to shock conditions in total magnetic field magnitude (B_{tot}) and bulk velocity magnitudes ($|v|$).

The automated detection method first smooths n_{ion} and B_{tot} burst mode data with a Savitzky-Golay filter with a zeroth order polynomial and 100 point window length. A sigmoid fitting function is applied to both parameters in 15 s windows that slide in 3 s intervals which returns the ratio $\frac{(\max - \min)}{\min}$ (hereafter we refer to this ratio as X where the subscript specifies which observable we are referring to), the epoch of the midpoint of the sigmoid fit, and whether the spacecraft is going from upstream to downstream or downstream to upstream ($d_{\uparrow\downarrow}$) by assessing whether the first fitted sigmoid value is less than the last fitted sigmoid value. Both parameter sigmoid fits must agree on $d_{\uparrow\downarrow}$ and both $X_{n_{ion}} \geq 0.4$ and $X_{B_{tot}} \geq 0.4$ to be initially selected.

The method then further filters the bow shock selection based on taking comparative ratios between the average component ion velocities and low energy ion spectra intensities 20 s to either side of the bow shock epoch but excluding the 5 s on either side closest to the boundary. We calculate the average component velocity in these windows, calculate the ion velocity magnitude, and set a threshold of $X_{|v|} \geq 0.3$. Similarly, for the ion spectra we first find the energy channel with the maximum intensity at the designated bow shock epoch. In order to avoid contamination based on ion energy peak widths, we select our maximum energy channel three energy channels lower than this peak intensity energy channel. We calculate the sum of ion energy intensity (I) from the lowest energy channel to our selected maximum energy channel. The average of the sums is calculated for 20 s on both sides of the bow shock epoch, but excludes the 5 s on both sides closest to the boundary. This is effectively a check to determine if the ion spectra is changing from beamed (solar wind or ion foreshock) to widely dispersed (magnetosheath). We set at threshold of $X_{\overline{\sum I}} \geq 0.03$. All thresholds are tuned through manual inspection.

If there are bow shocks identified within ±30 s with the same $d_{\uparrow\downarrow}$, we combine the bow shocks into a single epoch where $X_{n_{ion}}$ is the largest. Likewise, we combine bow shock epochs that are within ±0.5 s of each other regardless of whether they share the same $d_{\uparrow\downarrow}$.

The automated process is performed on each selected burst window independently on each MMS probe data set. In order for a bow shock to be included in our curated data set, we manually reviewed all the bow shocks identified from MMS2. From that curated list, the nearest bow shock in the remaining three probes is assigned as the matching bow shock. For each bow shock, the spacecraft location is determined by interpolating the MEC survey data to the bow shock epoch of each probe. Therefore, for each identified bow shock we have the epoch and the location at the time of the epoch for each probe.

Figure 1 shows an example of a quasi-perpendicular bow shock crossing on 7 October 2017 ($Q = 0.94$) where the bow shock location is automatically selected for each probe. The black vertical lines on the bottom four plots show the bow shock location that the automated sigmoid method selects. In this example, all four MMS probes pass from magnetosheath to solar wind in rapid succession due to the small distance between spacecraft. The bow shock epochs are primarily selected by the ion number density and confirmed by the other parameters exceeding the thresholds described above. This example is the 4th bow shock in our detailed shock list described in Section 5.

3.2. Method 2: Cross-Correlation Bow Shock Identification

Using the manually reviewed MMS2 crossings, we apply an alternative automatic bow shock detection method in the remaining MMS probes. Specifically, we perform a cross-correlation process on magnetic field magnitude for each MMS probe against MMS2. Then, we maximize the correlation coefficient when shifting up to 30 s in either direction. This method is predicated on having a detection from Method 1 (described in Section 3.1) and verified by manual review and due to this assumption, MMS2 bow shock epochs are co-located with either method.

Figure 1 shows the automated cross-correlation bow shock epochs in dashed vertical lines on the bottom four plots alongside the bow shock epochs determined from Method 1. There are deviations in the bow shock ramp locations based on the automated sigmoid method (MMS1: 12:07:12.39, MMS2: 12:07:12.80, MMS3: 12:07:13.73, MMS4: 12:07:12.19) and the automated cross-correlation method (MMS1: 12:07:12.72, MMS2: 12:07:12.80, MMS3: 12:07:12.86, MMS4: 12:07:12.76).

While there are advantages and disadvantages of both methods, discrepancies between the two methods can occur primarily be due to two reasons. The first reason is that in order to capture all bow shock crossings across our data set, we defined a window large enough to include wide/slower crossings. Therefore, the cross-correlation method uses 30 s windows on either side of the initial MMS2 crossing. This means that for narrow/fast bow shock crossings the correlation coefficient is dominated by the relatively calm regions surrounding the bow shock crossing rather than bow shock ramp leading to similar bow shock locations across all four probes. The second reason is because the sigmoid method is predicated on detecting variability in the bow shock ramp to identify the bow shock crossing location. This means that the variability between the four probes is dominated by the bow shock ramp region rather than surrounding environments. Due to these potential discrepancies, we include both methods throughout our analysis.

3.3. MMS Four Point Timing Analysis

Four-point timing analysis (Paschmann & Daly, 1998), as prescribed in Appendix 2 of D. L. Turner et al. (2021), enables calculating both the shock speed and bow shock normal using a simple formula:

$$\Delta t = (\mathbf{v_{sh}})^{-1} \Delta \mathbf{X} \tag{1}$$

where Δt is the difference in the bow shock ramp epoch between two spacecraft and $\Delta \mathbf{X}$ is the difference in spacecraft position at the bow shock ramp epoch for the same spacecraft. $\mathbf{v_{sh}}$, the shock velocity vector, can also

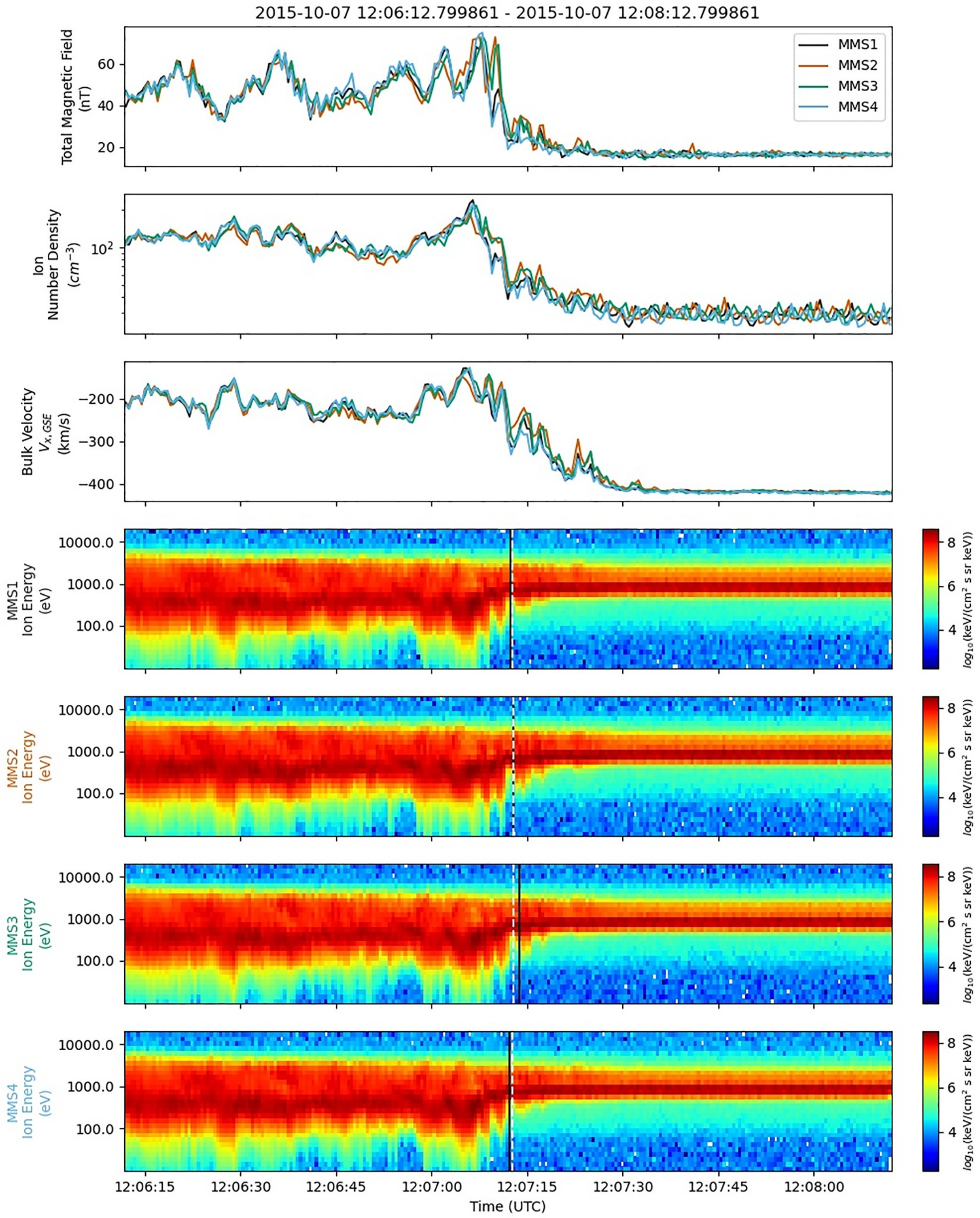

Figure 1. An example of an automatically detected bow shock in all four MMS probes on 7 October 2015. Data is shown at 500 ms resolution but analysis is done at the resolution of the Level 2 data. In the top three panels the MMS probes (MMS1 in black, MMS2 in orange, MMS3 in green, and MMS4 in blue) are shown for each quantity. From top to bottom, we show the quantities that are used in the automated detection method: total magnetic field magnitude, ion number density, bulk velocity (note that we only show $V_{x,GSE}$ but we use all components), and the bottom four plots show the ion spectra for each MMS probe. The black vertical lines in the bottom four plots show the sigmoid automatically selected bow shock epoch for each MMS probe while the dashed white vertical lines show the cross-correlation bow shock epochs.

be described instead by its components, $v_{sh}\mathbf{n_{sh}}$, where v_{sh} is the shock speed and $\mathbf{n_{sh}}$ is the bow shock normal. While only three combination pairs are required to solve the equation and calculate bow shock normals, using all six combination pairs of the four MMS probes enables uncertainty estimates of the parameters.

10.1029/2025JA034252

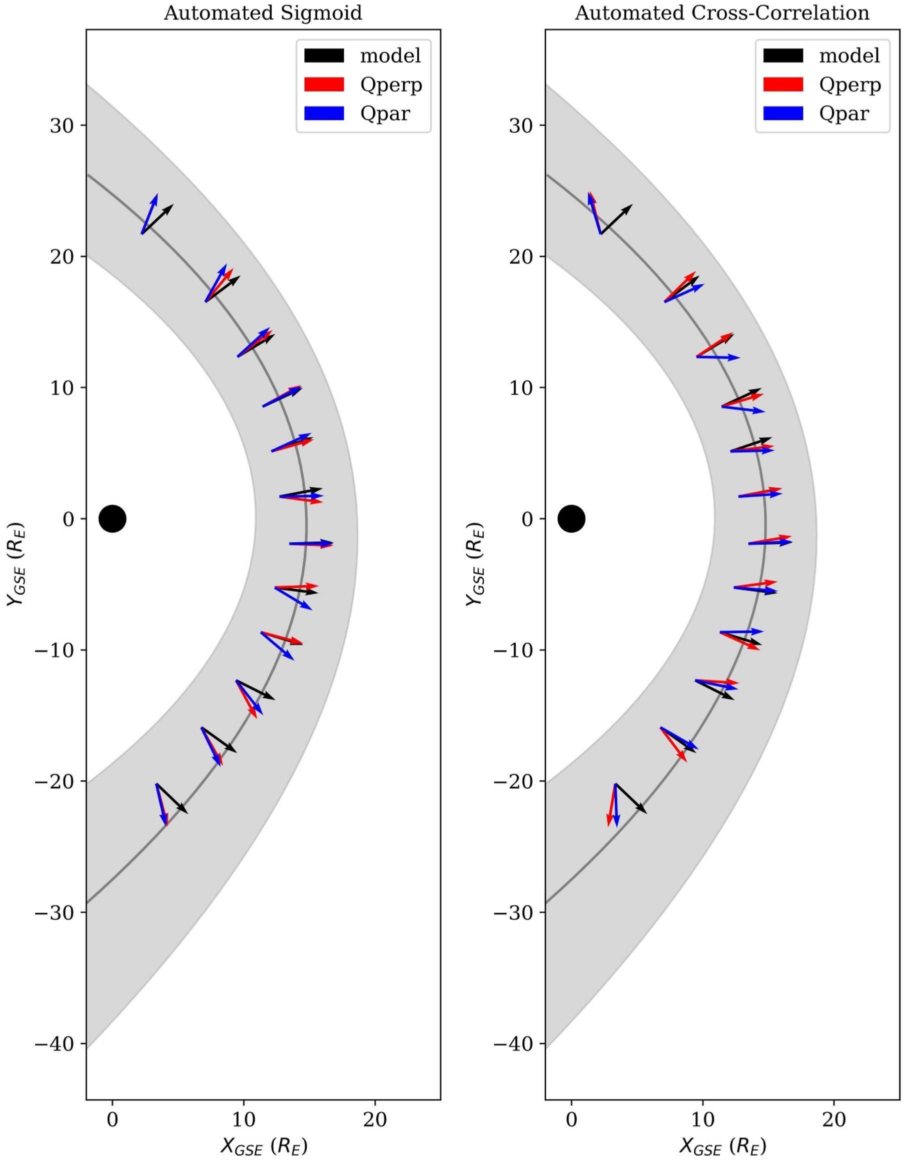

Figure 2. The average bow shock normal from four point timing for Qperp (red arrows) and Qpar (blue arrows) bow shocks by local time hour sectors. The arrow tail location is the position of the average bow shock location for that particular sector. The Yeakel et al. (2025) model at 45° IMF angle (black arrow) for the mean sector locations is shown for comparison. The overall mean Yeakel et al. (2025) model (gray line) and the 95% model confidence interval (shaded gray) are overlaid. The bow shock averages are shown for Method 1 (left) and Method 2 (right).

We apply this method to both methods discussed above. Four-point timing has an arbitrary sign allowing the shock's normal vector to be Earthward or anti-Earthward. In order to compare with models, we always require that the normal faces outwards (i.e., anti-Earthward).

We additionally calculate θ_{Bn} using the angle between the bow shock normal and the average magnetic field vector 20 s upstream of the bow shock epoch and exclude the 5 s nearest to the bow shock epoch.

4. Results

4.1. Comparison of Bow Shock Normal to Model

Figure 2 shows the average bow shock normals in local time hour sectors from the four point timing, with location and times obtained from both automated methods. The arrows show the normal from the mean Yeakel

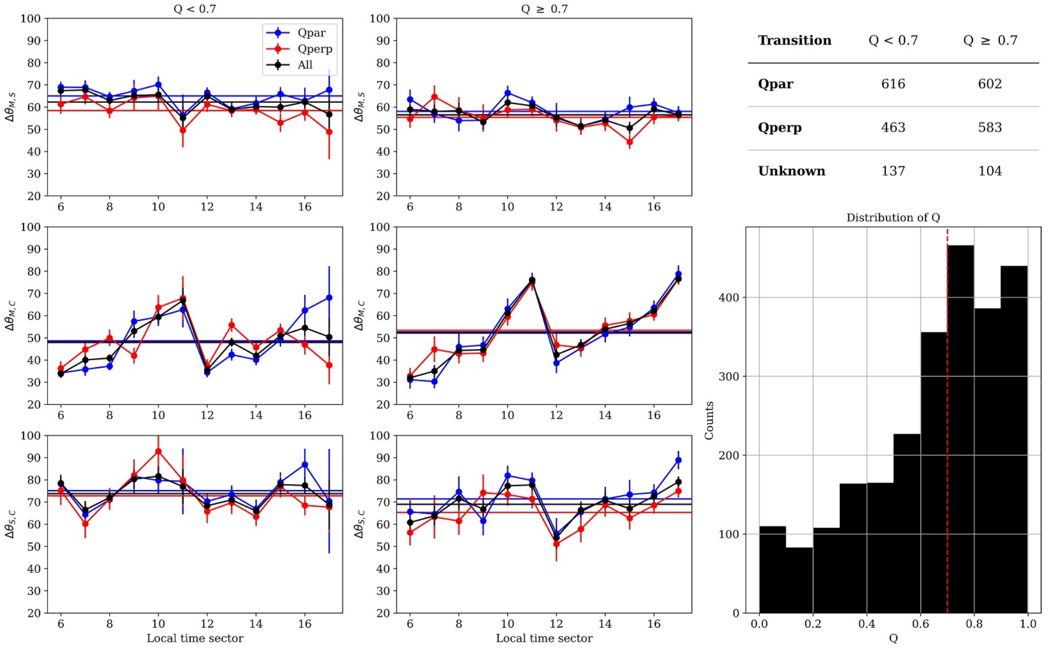

Transition	Q < 0.7	Q ≥ 0.7
Qpar	616	602
Qperp	463	583
Unknown	137	104

Figure 3. The angle between the Yeakel et al. (2025) model, Method 1, and Method 2 at the MMS2 location of each bow shock. The first two columns show the breakdown based on tetrahedron quality thresholds and the third column shows the distribution of Q and transition type. The histogram shows the Q threshold of 0.7 in a red dashed line. Note that some transitions were labeled as neither Qpar nor Qperp bow shocks, but are included in the total bow shocks. (top) Shows the angle between the model and Method 1, (middle) shows the angle between the model and Method 2, and (bottom) shows the angle between Method 1 and Method 2 by local time sector. The subscripts stand for model (M), Method 1–sigmoid (S), and Method 2–cross-correlation (C). In each plot, the angle difference is shown for all bow shocks (black), all Qperp bow shocks (red), and all Qpar bow shocks (blue) where the error bars represent the standard error. The horizontal lines are the mean angle for the respective bow shock populations.

et al. (2025) model at 45° IMF angle (black), for Qperp crossings (red), and for Qpar ones (blue) at the mean location of all bow shocks taken from MMS2 within the sector projected in the X-Y plane. Overlaid in gray is the 95% bow shock confidence interval from the Yeakel et al. (2025) model at 45° IMF angle. The bow shock mean locations tend to be inward of the model mean as our observations skew towards solar maximum and because the majority of the bow shocks are observed at high Z values ($Z > 2R_E$). This provides an overall view of the bow shock normal orientations. Qualitatively, the average normal vector derived from hundreds of samples produces a physically consistent picture, showing the expected transition from the subsolar region to the flanks. However, the cross-correlation method appears to introduce greater variability at the flanks, and for both methods, the variability between Qpar and Qperp shock orientations is significant.

4.2. Comparison of Multi Spacecraft Timing Methods

In order to properly investigate and understand how each bow shock normal method deviates from one another, we calculate the individual angles between the model, Method 1, and Method 2 and display how these values change based on local time sector. This is shown in Figure 3, where the difference angle ($\Delta\theta$) is calculated for each bow shock crossing. To further evaluate our data set, we perform the same analysis for two different tetrahedron quality configurations (Q). It is necessary to first exclude bow shocks that are taken during MMS's "string of pearls" configuration (24 January 2019–14 March 2019) which reduces our bow shock count to 2,513 (8 of which have no Q values). The top panels show the angle between Method 1 and the model, the middle panels show the angle between Method 2 and the model, and the bottom panels show the angle between Method 1 and 2. The first column describes the difference under low Q values while the second column shows high Q values. The third column shows the number of Qpar and Qperp bow shocks that are split fairly evenly even when considering the Q thresholds. The histogram shows the distribution of Q with our threshold of 0.7 overlaid in red. The choice of 0.7 was made because, by design, the MMS mission is expected to have $Q > 0.7$ for 80% of the time when the spacecraft are in the science region of interest (Fuselier et al., 2014). However, as shown here, this does not

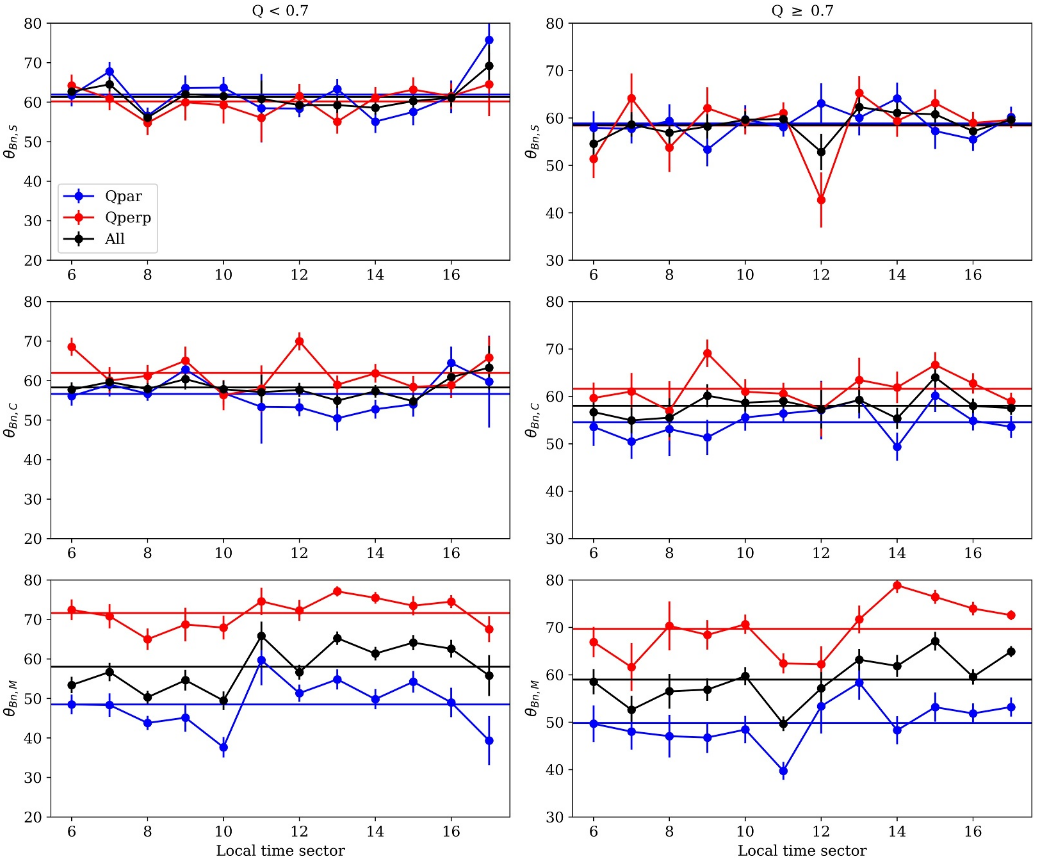

Figure 4. The angle between the IMF vector and Method 1–sigmoid ($\theta_{Bn,S}$, top), Method 2–cross-correlation ($\theta_{Bn,C}$, middle), and Yeakel et al. (2025) model ($\theta_{Bn,M}$, bottom) bow shock normals at the MMS2 location of each bow shock. In each plot, all bow shocks (black), Qperp bow shocks (red), and Qpar bow shocks (blue) are shown for each local time sector where the error bars represent the standard error. The horizontal lines are the mean angle for the respective bow shock population.

necessarily hold for bow shock crossings, where approximately half of the events correspond to $Q < 0.7$. This deviation may significantly impact multi-spacecraft techniques, regardless of the spatial scales of the phenomena being investigated. Comparing now Figure 3 with the average picture shown in Figure 2, we see that despite the reasonable bow shock normals in the average position, the individual bow shock deviations differ by $\sim 50 - 60°$ irrespective of tetrahedron quality factor.

4.3. Comparison of θ_{Bn} Across MLT

In order to get further insights, we plot θ_{Bn} using the model, Method 1, and Method 2 bow shock normal with the IMF vector described in Section 3.3 in Figure 4. From top to bottom we plot the θ_{Bn} for Method 1, Method 2, and the bow shock model for Q < 0.7 (left) and Q ≥ 0.7 (right). Here we can see that the locally measured θ_{Bn} from both multi-spacecraft approaches correspond to higher, almost exclusive Qperp crossings. Interestingly, apart from the subset of $Q \geq 0.7$ with four-point timing, it also seems that the Qpar crossings (reminder that our Qpar shocks here are classified by the presence of an ion foreshock upstream of the crossing), locally, produce similar geometries to the Qperp crossings. On the other hand, looking at the modeled angles, we see a global configuration that is closer to our expectation with a significant difference between Qpar and Qperp shocks in terms of shock geometries. An important consideration in Figure 4 is that the results can be partially influenced by the automatic selection of the upstream magnetic field. The current method uses a 20-s window (excluding 5 s closest to the shock ramp), which is intended to smooth out high-frequency wave variability (e.g., whistlers). However, this approach does not account for the possible presence of low-frequency waves or upstream transients (Kajdič et al., 2024; Zhang et al., 2022). A future analysis is planned to quantify the impact of the upstream magnetic field selection, including a comparison with undisturbed solar wind magnetic field from data sets such as OMNIweb.

This will help assess the influence of this parameterization and determine whether it contributes towards any systematic bias.

5. Discussion and Conclusions

During our analysis, we found that MMS does not achieve ion-inertial-scale separations with a high tetrahedron quality factor ($Q > 0.7$) at any time during a bow shock crossing, limiting its ability to resolve shock structures at these scales. The bow shock crossings primarily occur at electron-scale separations (∼20–80 km, i.e., less than an ion inertial length). However, when evaluating multi-spacecraft timing at electron-scale separations, we observe a systematic increase in θ_{Bn}. Additionally, under high tetrahedron quality, the differences between timing methods decrease slightly (Figure 3), and the derived shock geometries align more closely with our expectations based on the Qpar and Qperp classifications inferred from ion foreshock measurements (Figure 4).

This suggests that while ion kinetic scales primarily govern shock geometry, electron-scale phenomena can influence local shock properties. On global scales (represented by modeled shock properties) we observe a clearer distinction between Qpar and Qperp shocks. As tetrahedron quality improves, MMS measurements are slightly better aligned with these global expectations. However, high tetrahedron quality alone does not guarantee accurate measurements. Given that approximately half of the observed crossings occur with $Q < 0.7$, studies focusing on electron-scale phenomena at the shock, such as electron-only reconnection (Guo et al., 2023; Ng et al., 2022; Phan et al., 2018) and wave-particle interactions (He et al., 2022; Li et al., 2025; Wang et al., 2023), should interpret their results with particular caution. Furthermore, since MMS operates at electron scales, the presence of upstream whistler waves in both Qpar and Qperp shocks could influence the timing results, leading to more uniform θ_{Bn} estimates skewed towards Qperp regime (Baumjohann & Treumann, 2012).

Overall, even when $Q \geq 0.7$, the timing method yields an average θ_{Bn} of approximately 60°, indicating a systematic shift in shock characterization. Specifically, Qperp shocks appear less perpendicular, while Qpar shocks appear more perpendicular when using the timing method. The latter aligns with the idea that (Qpar) shocks can exhibit more perpendicular characteristics locally due to the presence of upstream out-of-plane waves (Baumjohann & Treumann, 2012; Hull et al., 2012; Scholer et al., 2003), while also indicating that ion foreshock can be found in shocks that are in oblique shock configurations (Karlsson et al., 2021). The former, however, is unexpected and may suggest a systematic issue with using the timing method to characterize local shock geometry in electron scale, resulting in a systematic result that is not necessarily physically accurate.

Examining all shocks, our findings support prior studies (Gingell et al., 2017; Johlander et al., 2016; Lalti et al., 2022) that questioned the reliability of multi-spacecraft timing for robust shock characterization. While this issue may be known, it has not yet been fully addressed statistically. Ultimately, without contextual knowledge, such as the presence of a foreshock, local MMS multi-spacecraft timing alone appears insufficient for accurately determining shock geometry. Future mission concepts, such as the Plasma Observatory (Retinò et al., 2022), should consider this limitation and ensure that their multi-spacecraft approach ($N > 4$) has sufficient separations to capture ion-scale structures while maintaining tight formation on other probes to obtain electron scale properties. Finally, bow shock-specific mission concepts like the Multi-point Assessment of the Kinematics of Shocks (MAKOS; Goodrich et al., 2023) should also consider such limitations.

A key direction for future work is to investigate the dependence of these results on the upstream magnetic field. In our case, we used local in situ measurements for capturing the magnetic field, which due to their variability can have a significant effect on the calculation. Additionally, a crucial next step in comparing modeled and spacecraft-derived shock normals, representing global versus local perspectives, is to identify conjunctions with other missions (e.g., THEMIS, Cluster) that probe ion-scale lengths. During such conjunction events the evaluation of shock geometries can be made across multiple scales, removing any ambiguity regarding the governing dynamics involved.

In summary, our analysis demonstrates that local multi-spacecraft timing yields systematically higher θ_{Bn} values. Reduced discrepancies are found during high tetrahedron formation but significant deviations from global, model-driven shock geometries persist. These results underscore the limitations of relying solely on local measurements for shock characterization, particularly when contextual information, such as the presence of a foreshock or a similarly disturbed downstream magnetosheath, is missing. Ultimately, our automated methodology produces a comprehensive data set comprising thousands of high-resolution burst-mode bow shock crossings, which we make available to the community (see Section 5) for further scientific research which can be used for conjunction studies and for paving the way to future mission design and science objectives.

Conflict of Interest

The authors declare no conflicts of interest relevant to this study.

Data Availability Statement

The data used in this work is publicly available through the MMS Science Data Center and is available at https://lasp.colorado.edu/mms/sdc/public/. The labeled bow shock list with the detailed timing and spatial location of each shock ramp alongside the bow shock normal for the three methods produced in this work is available on Zenodo (Toy-Edens et al., 2025) at https://zenodo.org/records/15318626.

Acknowledgments

This work was funded by the NSF Geospace Environment Modeling (GEM) Grant 2225463 and NASA Grant 80NSSC24K0173. S.R. acknowledges the support by Johns Hopkins University Applied Physics Laboratory independent R&D fund and the MMS Early Career Award 80NSSC25K7353. We utilized HelioCloud platform (Thomas et al., 2022) for part of our computation and thank the HelioCloud team for their support.

References

Balogh, A., & Treumann, R. A. (2013). *Physics of collisionless shocks: Space plasma shock waves*. Springer Science and Business Media.

Baumjohann, W., & Treumann, R. A. (2012). *Basic space plasma physics*. World Scientific.

Bergman, S., Karlsson, T., Wong Chan, T., & Trollvik, H. (2025). Statistical properties of short large-amplitude magnetic structures (slams) in the foreshock of earth from cluster measurements. *Journal of Geophysical Research: Space Physics*, *130*(3), e2024JA033568. https://doi.org/10.1029/2024ja033568

Burch, J. L., Moore, T. E., Torbert, R. B., & Giles, B. L. (2015). Magnetospheric multiscale overview and science objectives. *Space Science Reviews*, *199*(1–4), 5–21. https://doi.org/10.1007/s11214-015-0164-9

Caprioli, D., & Spitkovsky, A. (2014). Simulations of ion acceleration at non-relativistic shocks. i. acceleration efficiency. *The Astrophysical Journal*, *783*(2), 91. https://doi.org/10.1088/0004-637x/783/2/91

Chapman, J. F., & Cairns, I. H. (2003). Three-dimensional modeling of Earth's bow shock: Shock shape as a function of Alfvén Mach number. *Journal of Geophysical Research (Space Physics)*, *108*(A5), 1174. https://doi.org/10.1029/2002JA009569

Eastwood, J., Lucek, E., Mazelle, C., Meziane, K., Narita, Y., Pickett, J., & Treumann, R. (2005). The foreshock. *Space Science Reviews*, *118*, 41–94.

Fuselier, S. A., Lewis, W. S., Schiff, C., Ergun, R., Burch, J. L., Petrinec, S. M., & Trattner, K. J. (2014). Magnetospheric multiscale science mission profile and operations. *Space Science Reviews*, *199*(1–4), 77–103. https://doi.org/10.1007/s11214-014-0087-x

Gingell, I., Schwartz, S. J., Burgess, D., Johlander, A., Russell, C. T., Burch, J. L., et al. (2017). MMS observations and hybrid simulations of surface ripples at a marginally quasi-parallel shock. *Journal of Geophysical Research: Space Physics*, *122*(11), 11-003. https://doi.org/10.1002/2017ja024538

Goodrich, K., Cohen, I. J., Schwartz, S., Wilson III, L. B., Turner, D., Caspi, A., et al. (2023). The multi-point assessment of the kinematics of shocks (MAKOS). *Frontiers in Astronomy and Space Sciences*, *10*, 1199711. https://doi.org/10.3389/fspas.2023.1199711

Guo, A., Lu, Q., Lu, S., Wang, S., & Wang, R. (2023). Properties of electron-scale magnetic reconnection at a quasi-perpendicular shock. *The Astrophysical Journal*, *955*(1), 14. https://doi.org/10.3847/1538-4357/acec48

He, J., Zhu, X., Luo, Q., Hou, C., Verscharen, D., Duan, D., et al. (2022). Observations of rapidly growing whistler waves in front of space plasma shock due to resonance interaction between fluctuating electron velocity distributions and electromagnetic fields. *The Astrophysical Journal*, *941*(2), 147. https://doi.org/10.3847/1538-4357/ac9ea9

Henderson, M. G., Morley, S. K., & Burch, J. L. (2022). MMS 4 Magnetic Ephemeris and Coordinates (MEC) and support (Tsyganenko 1989 model, dynamic conditions), level 2 (L2), survey mode, 30 s data. *NASA Space Physics Data Facility*. https://doi.org/10.48322/552N-ER81

Hull, A., Muschietti, L., Oka, M., Larson, D., Mozer, F., Chaston, C., et al. (2012). Multiscale whistler waves within Earth's perpendicular bow shock. *Journal of Geophysical Research: Space Physics*, *117*(A12). https://doi.org/10.1029/2012ja017870

Johlander, A., Battarbee, M., Turc, L., Ganse, U., Pfau-Kempf, Y., Grandin, M., et al. (2022). Quasi-parallel shock reformation seen by magnetospheric multiscale and ion-kinetic simulations. *Geophysical Research Letters*, *49*(2), e2021GL096335. https://doi.org/10.1029/2021GL096335

Johlander, A., Schwartz, S., Vaivads, A., Khotyaintsev, Y. V., Gingell, I., Peng, I., et al. (2016). Rippled quasiperpendicular shock observed by the magnetospheric multiscale spacecraft. *Physical Review Letters*, *117*(16), 165101. https://doi.org/10.1103/physrevlett.117.165101

Kajdič, P., Blanco-Cano, X., Turc, L., Archer, M., Raptis, S., Liu, T. Z., et al. (2024). Transient upstream mesoscale structures: Drivers of solar-quiet space weather. *Frontiers in Astronomy and Space Sciences*, *11*, 1436916. https://doi.org/10.3389/fspas.2024.1436916

Karlsson, T., Raptis, S., Trollvik, H., & Nilsson, H. (2021). Classifying the magnetosheath behind the quasi-parallel and quasi-perpendicular bow shock by local measurements. *Journal of Geophysical Research: Space Physics*, *126*(9), e2021JA029269. https://doi.org/10.1029/2021ja029269

King, J. H., & Papitashvili, N. E. (2005). Solar wind spatial scales in and comparisons of hourly Wind and ACE plasma and magnetic field data. *Journal of Geophysical Research (Space Physics)*, *110*(A2), A02104. https://doi.org/10.1029/2004JA010649

Koller, F., Raptis, S., Temmer, M., & Karlsson, T. (2024). The effect of fast solar wind on ion distribution downstream of Earth's bow shock. *The Astrophysical Journal Letters*, *964*(1), L5. https://doi.org/10.3847/2041-8213/ad2ddf

Lalti, A., Khotyaintsev, Y. V., Dimmock, A. P., Johlander, A., Graham, D. B., & Olshevsky, V. (2022). A database of mms bow shock crossings compiled using machine learning. *Journal of Geophysical Research: Space Physics*, *127*(8), e2022JA030454. https://doi.org/10.1029/2022ja030454

Li, J.-H., Zhou, X.-Z., Liu, Z.-Y., Wang, S., Omura, Y., Li, L., et al. (2025). Direct observations of cross-scale wave-particle energy transfer in space plasmas. *Science Advances*, *11*(6), eadr8227. https://doi.org/10.1126/sciadv.adr8227

Liu, T. Z., Hao, Y., Wilson III, L. B., Turner, D. L., & Zhang, H. (2021). Magnetospheric multiscale observations of earth's oblique bow shock reformation by foreshock ultralow-frequency waves. *Geophysical Research Letters*, *48*(2), e2020GL091184. https://doi.org/10.1029/2020gl091184

Ng, J., Chen, L.-J., Bessho, N., Shuster, J., Burkholder, B., & Yoo, J. (2022). Electron-scale reconnection in three-dimensional shock turbulence. *Geophysical Research Letters*, *49*(15), e2022GL099544. https://doi.org/10.1029/2022gl099544

Park, J., Caprioli, D., & Spitkovsky, A. (2015). Simultaneous acceleration of protons and electrons at nonrelativistic quasiparallel collisionless shocks. *Physical Review Letters*, *114*(8), 085003. https://doi.org/10.1103/physrevlett.114.085003

Paschmann, G., & Daly, P. W. (1998). Analysis methods for multi-spacecraft data. ISSI Scientific Reports Series SR-001, ESA/ISSI (Vol. *1*).

Phan, T., Eastwood, J. P., Shay, M., Drake, J., Sonnerup, B. Ö., Fujimoto, M., et al. (2018). Electron magnetic reconnection without ion coupling in Earth's turbulent magnetosheath. *Nature*, *557*(7704), 202–206. https://doi.org/10.1038/s41586-018-0091-5

Pollock, C., Moore, T., Jacques, A., Burch, J., Gliese, U., Saito, Y., et al. (2016). Fast plasma investigation for magnetospheric multiscale. *Space Science Reviews*, *199*(1), 331–406. https://doi.org/10.1007/s11214-016-0245-4

Raptis, S., Aminalragia-Giamini, S., Karlsson, T., & Lindberg, M. (2020). Classification of magnetosheath jets using neural networks and high resolution OMNI (HRO) data. *Frontiers in Astronomy and Space Sciences*, *7*, 24. https://doi.org/10.3389/fspas.2020.00024

Raptis, S., Karlsson, T., Plaschke, F., Kullen, A., & Lindqvist, P.-A. (2020). Classifying magnetosheath jets using mms: Statistical properties. *Journal of Geophysical Research: Space Physics*, *125*(11), e2019JA027754. https://doi.org/10.1029/2019ja027754

Raptis, S., Karlsson, T., Vaivads, A., Pollock, C., Plaschke, F., Johlander, A., et al. (2022). Downstream high-speed plasma jet generation as a direct consequence of shock reformation. *Nature Communications*, *13*(1), 598. https://doi.org/10.1038/s41467-022-28110-4

Raptis, S., Lalti, A., Lindberg, M., Turner, D. L., Caprioli, D., & Burch, J. L. (2025). Revealing an unexpectedly low electron injection threshold via reinforced shock acceleration. *Nature Communications*, *16*(1), 488. https://doi.org/10.1038/s41467-024-55641-9

Retinò, A., Khotyaintsev, Y., Le Contel, O., Marcucci, M. F., Plaschke, F., Vaivads, A., et al. (2022). Particle energization in space plasmas: Towards a multi-point, multi-scale plasma observatory. *Experimental Astronomy*, *54*(2), 427–471. https://doi.org/10.1007/s10686-021-09797-7

Russell, C., Mellott, M., Smith, E., & King, J. (1983). Multiple spacecraft observations of interplanetary shocks: Four spacecraft determination of shock normals. *Journal of Geophysical Research*, *88*(A6), 4739–4748. https://doi.org/10.1029/ja088ia06p04739

Scholer, M., Kucharek, H., & Shinohara, I. (2003). Short large-amplitude magnetic structures and whistler wave precursors in a full-particle quasi-parallel shock simulation. *Journal of Geophysical Research: Space Physics*, *108*(A7). https://doi.org/10.1029/2002ja009820

Schwartz, S. J. (1998). Shock and discontinuity normals, mach numbers, and related parameters. *ISSI Scientific Reports Series*, *1*, 249–270.

Svenningsson, I., Yordanova, E., Khotyaintsev, Y. V., André, M., & Cozzani, G. (2025). Classifying the magnetosheath using local measurements from mms. *Journal of Geophysical Research: Space Physics*, *130*(1), e2024JA033272. https://doi.org/10.1029/2024ja033272

Thomas, B. A., Vandegriff, J. D., Antunes, A. K., Bradford, J. W., Yeakel, K., Mo, W., et al. (2022). HelioCloud: A community cloud-based approach to heliophysics analytics and software development. In *AGU fall meeting abstracts* (Vol. 2022).SH45B-01.

Torbert, R. B., Russell, C. T., Magnes, W., Ergun, R. E., Lindqvist, P.-A., LeContel, O., et al. (2014). The FIELDS instrument suite on MMS: Scientific objectives, measurements, and data products. *Space Science Reviews*, *199*(1–4), 105–135. https://doi.org/10.1007/s11214-014-0109-8

Toy-Edens, V. (2024). 8 years of dayside magnetospheric multiscale (mms) unsupervised clustering plasma regions classifications [Dataset]. *Zenodo*. https://doi.org/10.5281/ZENODO.10491878

Toy-Edens, V., Mo, W., Raptis, S., & Turner, D. L. (2024). Classifying 8 years of mms dayside plasma regions via unsupervised machine learning. *Journal of Geophysical Research: Space Physics*, *129*(6), e2024JA032431. https://doi.org/10.1029/2024JA032431

Toy-Edens, V., Raptis, S., Turner, D., Mo, W., & Young, S. (2025). Automated mms burst-mode bow shock locations and normals [Dataset]. *Zenodo*. https://doi.org/10.5281/ZENODO.15318625

Treumann, R. (2009). Fundamentals of collisionless shocks for astrophysical application, 1. Non-relativistic shocks. *Astronomy and Astrophysics Review*, *17*(4), 409–535. https://doi.org/10.1007/s00159-009-0024-2

Treumann, R. A., & Baumjohann, W. (1997). *Advanced space plasma physics*. Published by Imperial College Press and Distributed by World Scientific Publishing Co. https://doi.org/10.1142/p020

Trotta, D., Vuorinen, L., Hietala, H., Horbury, T., Dresing, N., Gieseler, J., et al. (2022). Single-spacecraft techniques for shock parameters estimation: A systematic approach. *Frontiers in Astronomy and Space Sciences*, *9*, 1005672. https://doi.org/10.3389/fspas.2022.1005672

Turner, D., Wilson III, L., Liu, T., Cohen, I., Schwartz, S., Osmane, A., et al. (2018). Autogenous and efficient acceleration of energetic ions upstream of earth's bow shock. *Nature*, *561*(7722), 206–210. https://doi.org/10.1038/s41586-018-0472-9

Turner, D. L., Wilson, L. B., Goodrich, K. A., Madanian, H., Schwartz, S. J., Liu, T. Z., et al. (2021). Direct multipoint observations capturing the reformation of a supercritical fast magnetosonic shock. *The Astrophysical Journal Letters*, *911*(2), L31. https://doi.org/10.3847/2041-8213/abec78

Wang, C., Huang, S., Yuan, Z., Jiang, K., Zhang, J., Dong, Y., & Xiong, Q. (2023). In situ observation of electron acceleration by a double layer in the bow shock. *The Astrophysical Journal*, *952*(1), 78. https://doi.org/10.3847/1538-4357/acdacb

Wilson III, L. B., Sibeck, D. G., Turner, D. L., Osmane, A., Caprioli, D., & Angelopoulos, V. (2016). Relativistic electrons produced by foreshock disturbances observed upstream of earth's bow shock. *Physical Review Letters*, *117*(21), 215101. https://doi.org/10.1103/physrevlett.117.215101

Wilson III, L., Koval, A., Sibeck, D., Szabo, A., Cattell, C., Kasper, J., et al. (2013). Shocklets, slams, and field-aligned ion beams in the terrestrial foreshock. *Journal of Geophysical Research: Space Physics*, *118*(3), 957–966. https://doi.org/10.1029/2012ja018186

Yeakel, K. L., Cohen, I., & Turner, D. L. (2025). Variability of earth's magnetopause and bow shock locations modeled via multi-decade solar wind observations. *Geophysical Research Letters*, *52*(10), e2025GL115462. https://doi.org/10.1029/2025gl115462

Zhang, H., Zong, Q., Connor, H., Delamere, P., Facskó, G., Han, D., et al. (2022). Dayside transient phenomena and their impact on the magnetosphere and ionosphere. *Space Science Reviews*, *218*(5), 40. https://doi.org/10.1007/s11214-021-00865-0